

# Seq-DeepIPC: Sequential Sensing for End-to-End Control in Legged Robot Navigation

Oskar Natan, *Member, IEEE*, and Jun Miura, *Member, IEEE*

**Abstract**— We present Seq-DeepIPC, a sequential end-to-end perception-to-control model for legged robot navigation in real-world environments. Seq-DeepIPC advances intelligent sensing for autonomous legged navigation by tightly integrating multi-modal perception (RGB-D + GNSS) with temporal fusion and control. The model jointly predicts semantic segmentation and depth estimation, giving richer spatial features for planning and control. For efficient deployment on edge devices, we use EfficientNet-B0 as the encoder, reducing computation while maintaining accuracy. Heading estimation is simplified by removing the noisy IMU and instead computing the bearing angle directly from consecutive GNSS positions.

We collected a larger and more diverse dataset that includes both road and grass terrains, and validated Seq-DeepIPC on a robot dog. Comparative and ablation studies show that sequential inputs improve perception and control in our models, while other baselines do not benefit. Seq-DeepIPC achieves competitive or better results with reasonable model size; although GNSS-only heading is less reliable near tall buildings, it is robust in open areas. Overall, Seq-DeepIPC extends end-to-end navigation beyond wheeled robots to more versatile and temporally-aware systems. To support future research, we will release the codes to our GitHub repository at <https://github.com/oskarnatan/Seq-DeepIPC>.

**Index Terms**— end-to-end navigation, sequential perception, legged robot autonomy, multi-task learning, RGB-D vision

arXiv:2510.23057v1 [cs.RO] 27 Oct 2025

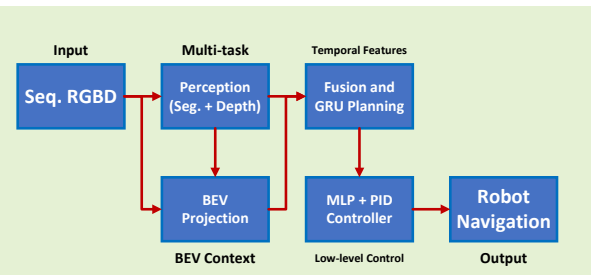
## I. INTRODUCTION

Modern robotic navigation systems increasingly favor end-to-end learning architectures, which directly map raw sensory data to control commands. This approach reduces the need for hand-engineered modules and allows shared features and joint optimization across tasks [1] [2]. Using this strategy, we can minimize information loss as the systems can learn all by itself. However, real-world deployment of such systems is still fraught with challenges: sensor noise, localization drift, dynamic environments, and variable terrain all undermine performance [3] [4]. Moreover, resource constraints on embedded platforms often limit how expressive or deep such models can be. In many robotics settings, especially outdoors or on mobile agents, these issues degrade navigation performance and robustness [5] [6]. From a sensing perspective, the challenge lies in converting multi-modal, noisy sensor streams into consistent spatial representations that can guide control reliably in unstructured environments.

To address these challenges, recent methods have incorporated multi-task supervision, sensor fusion, and temporal modeling [7] [8]. For example, Huang et al. fuse RGB and depth at early or late stages to enhance spatial understanding [9], other model called AIM-MT [10] encourages the network

Oskar Natan (corresponding author) is with the Department of Computer Science and Electronics, Universitas Gadjah Mada, Yogyakarta Indonesia, Email: oskarnatan@ugm.ac.id

Jun Miura is with the Department of Computer Science and Engineering, Toyohashi University of Technology, Toyohashi Japan. Email: jun.miura@tut.jp



to learn auxiliary tasks (semantic segmentation and depth estimation) to improve its latent representations. Our previous work, DeepIPC, made strides by coupling segmentation-guided feature extraction with waypoint-driven control in a compact architecture, demonstrating real-world drivability on a wheeled platform [11]. However, three persistent gaps remain: (i) single-frame perception is susceptible to aliasing and temporal inconsistency; (ii) reliance on IMU-based heading estimation introduces drift, magnetic interference, and hardware complexity; (iii) most existing systems are validated on wheeled robots navigating structured roads, limiting generality to more challenging surfaces.

In this paper, we present Seq-DeepIPC as a continuation and improvement of DeepIPC. Our model ingests short sequences of RGB-D frames, producing temporally consistent features, and jointly estimates semantic segmentation + depth to enable stronger spatial reasoning. We replace heavier encoders with EfficientNet-B0, facilitating real-time inference on constrained platforms [12] [13]. Rather than using a noisy IMU, we compute bearing angle from consecutive GNSS fixes via a geodesic formula, which improves heading stability in open terrain. We evaluate the system on a larger campus loop than in DeepIPC, under mixed road and grass terrains, and deploy it on a legged robot to test its generalization beyond wheeled navigation. In comparative and ablation studies (varying sequence lengths, comparing with Huang et al. [9] and AIM-MT [10] baselines), we demonstrate that only our DeepIPC-derived models benefit from temporal input, achieving consistent gains in perception and control, with trade-offs in inference speed.

Our key novelties are:

- 1) Temporal integration through sequential RGB-D input, improving perception consistency under motion. This includes dual-head perception (segmentation + depth) to enrich spatial features for planning.
- 2) Edge-compatible design via EfficientNet-B0 encoders and IMU-free bearing estimation via GNSS-only geodesic formula.
- 3) Deployment and evaluation on a legged robot navigating both road and grass in a larger-scale environment.

## II. RELATED WORKS

### A. End-to-End Learning for Robot Navigation

End-to-end navigation learns a direct mapping from raw onboard sensors to control, bypassing modular stacks. Recent works have advanced imitation- and reinforcement-learning formulations, sensor fusion, and decoder design. Ishihara *et al.* introduced an attention-based multi-task policy (AIM-MT) that couples perception heads with driving commands inside a conditional imitation framework [14]. Hou and Zhang showed that by adding safety information into the probabilistic graphical model(PGM) and learning it in conjunction with the reinforcement learning process can solve multiple driving tasks [15]. For non-vision modalities, Wang *et al.* demonstrated end-to-end navigation from raw LiDAR with robustness gains [16]. Transformer-based fusion has also become prominent: TransFuser integrates image and LiDAR features with self-attention and achieves state-of-the-art closed-loop results [17]. Decoder capacity and refinement have been explored, which stacks coarse-to-fine reasoning to stabilize planning under complex scenes [18]. These advances reduce hand-crafted intermediates and motivate our sequential and multi-task formulation.

### B. Sequential and Temporal Modeling

Temporal aggregation stabilizes perception and improves control under motion, occlusion, and noise. Attention-based fusion and recurrent encoders have been used to integrate multi-frame evidence for planning (e.g., TransFuser’s temporal fusion) [17]. Cross-modal temporal fusion strategies (e.g., CrossFuser) further refine multi-sensor features and improve downstream decision quality [19]. Policy-level fusion (PolicyFuser) combines complementary policies to exploit temporal context and multi-modality in closed loop [20]. Beyond specific architectures, recent studies formalize multi-camera BEV temporal fusion and contextual representation for end-to-end planning [21]. Other spatio-temporal pipelines such as DeepSTEP confirm that recurrent or transformer-based temporal integration can improve prediction robustness [22]. These directions motivate Seq-DeepIPC to fuse short RGB-D sequences via GRU, yielding temporally smoothed latent states that feed both waypoint and control heads.

### C. Legged Robot Navigation and Perception

Legged platforms introduce mixed-terrain challenges (grass, slopes, curb edges) and dynamic foothold constraints that differ from wheeled robots. Vision-aided frameworks have

shown that coupling perception with dynamic locomotion and planning can enable robust traversal over discrete or irregular terrain [23]. Vision-based navigation on small quadrupeds has also been demonstrated with lightweight pipelines suitable for onboard compute [24]. Recent systems for assistive or human-centric navigation push autonomy in real environments (e.g., RDog for BVI navigation) [25]. Surveys and reviews highlight rapid progress in learning-based legged locomotion and its perception stack [26]. Complementary work explores terrain-aware planning with vision (e.g., ViTAL), underlining the value of richer geometry for foothold selection and pose adaptation [27]. Our Seq-DeepIPC contributes to this space by unifying sequential RGB-D perception and control in a single end-to-end model *deployed on a legged robot*, and by validating mixed-terrain navigation (including grass) on campus-scale routes.

## III. METHODOLOGY

### A. Problem Statement

We study end-to-end navigation for a legged robot operating on mixed terrain. At each time  $t$ , the robot observes a short sequence of  $K$  multimodal frames

$$O_t = \{o_t, o_{t-1}, \dots, o_{t-K+1}\}, \quad o_i = (I_i^R, I_i^D), \quad (1)$$

where  $I_i^R$  and  $I_i^D$  are the RGB and depth images, respectively. In addition to sensory observations, the task is conditioned on a sequence of route points  $\mathcal{P}_t$  that prescribes the path from start to goal. Let

$$\mathcal{P}_t = \left\{ (\phi_t^{(m)}, \lambda_t^{(m)}) \right\}_{m=1}^M \quad (2)$$

denote the next  $M$  route points expressed in global latitude–longitude coordinates. During execution, the upcoming two points ( $M = 2$ ) are converted into local Cartesian coordinates and used both to guide the controller and to infer a discrete command (left/straight/right). The learning objective is to find parameters  $\theta$  of a function

$$f_\theta : (O_t, \mathcal{P}_t, g_t) \mapsto \{\hat{S}_t, \hat{D}_t, \hat{W}_t, u_t\}, \quad (3)$$

where  $g_t$  is the current GNSS measurement,  $\hat{S}_t$  and  $\hat{D}_t$  are the predicted semantic and depth maps,  $\hat{W}_t = \{\hat{w}_1, \dots, \hat{w}_N\}$  are the  $N = 5$  future waypoints in the local BEV frame, and  $u_t = (x, y, \theta)$  denotes the position–orientation control action.

In our dataset, the future waypoints  $\hat{W}_t$  are obtained from the robot’s ground-truth trajectory during data collection, where we consider up to five steps ahead for prediction. The control action  $u_t$  corresponds to the recorded remote control state that teleoperated the robot during data gathering. Training thus follows a supervised imitation learning paradigm: given a dataset

$$\mathcal{D} = \{(O_t, \mathcal{P}_t, g_t; S_t, D_t, W_t, u_t)\}_{t=1}^T, \quad (4)$$

we minimize the empirical risk

$$\min_{\theta} \frac{1}{T} \sum_{t=1}^T \mathcal{L}_{\text{total}}(\hat{S}_t, \hat{D}_t, \hat{W}_t, u_t; S_t, D_t, W_t, u_t), \quad (5)$$

where  $\mathcal{L}_{\text{total}}$  aggregates the task-specific losses. All outputs  $\{\hat{S}_t, \hat{D}_t, \hat{W}_t, u_t\}$  are defined in the local BEV frame whose origin is fixed at the robot base  $(0, 0)$ .

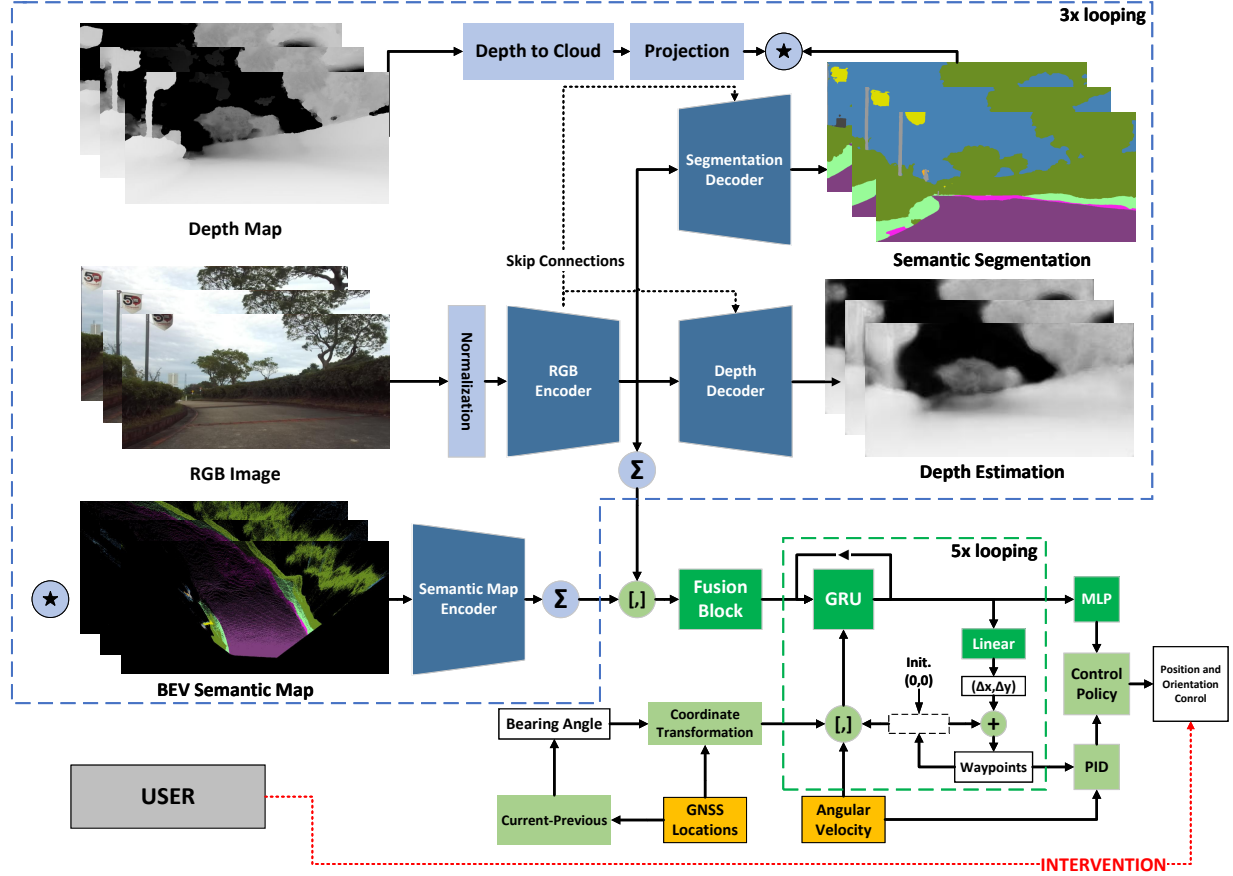


**Fig. 1:** Overview of the proposed Seq-DeepIPC architecture. (1) **Perception part:** Sequential RGB inputs are processed by an EfficientNet-B0 encoder, producing latent features that drive two prediction heads for semantic segmentation and depth estimation. The ground-truth depth maps are combined with predicted segmentation to generate BEV projections, which are further encoded by a second EfficientNet-B0 into BEV latent features. (2) **Planning and Control part:** The fused RGB and BEV latent features, together with transformed route points and bearing angle, are processed by a GRU to capture temporal dependencies. The resulting features drive two complementary control pathways: (a) PID controllers, which use predicted waypoints to estimate control signals, and (b) command-specific MLP controllers, which directly map the GRU latent space to  $(x, y, \theta)$  controls. The blended control policy regulates position and orientation for the legged robot.

## B. Proposed Model

Seq-DeepIPC consists of two main components: (i) a *perception part* that processes a short sequence of RGB-D observations and forms a BEV representation, and (ii) a *planning & control part* that infers future waypoints and control commands. An overview is shown in Fig. 1.

1) *Perception Part*: At time  $t$ , the perception branch receives a sequence of  $K$  RGB frames

$$O_t = \{o_t, o_{t-1}, \dots, o_{t-K+1}\}, \quad o_k = I_k^R, \quad (6)$$

where  $I_k^R$  denotes the  $k$ -th RGB image. Each frame is passed through a lightweight EfficientNet-B0 encoder to extract latent features  $f_k^R$ . From this shared latent space, two prediction heads output a semantic map  $\hat{S}_k$  and a depth map  $\hat{D}_k$ . While the predicted depth is not directly used for BEV construction, it serves as an auxiliary regression task that regularizes the encoder and enforces geometry-aware latent features.

**BEV construction.** Let  $\hat{S}_k \in [0, 1]^{H_{img} \times W_{img} \times C}$  be the per-pixel class scores and  $I_k^D \in \mathbb{R}^{H_{img} \times W_{img}}$  the ground-truth

depth. Back-project pixels with intrinsics  $\mathbf{K}$  and transform to the robot frame:

$$\mathbf{X}^r = \mathcal{T}_{c \rightarrow r}(\pi^{-1}(\mathbf{K}, I_k^D)) = \{(x_i, y_i, z_i)\}. \quad (7)$$

The BEV covers  $x \in (0, 16]$  m (forward) and  $y \in [-16, 16]$  m (left-right), with resolution  $H \times W = 128 \times 256$  so that  $\Delta_x = \frac{16}{128} = 0.125$  m and  $\Delta_y = \frac{32}{256} = 0.125$  m. Index each point to the BEV grid (robot at bottom-center):

$$i = \lfloor x_i / \Delta_x \rfloor, \quad j = \lfloor (y_i + 16) / \Delta_y \rfloor, \quad (i, j) \in [0, H-1] \times [0, W-1]. \quad (8)$$

Let  $\mathbf{e}_c \in \{0, 1\}^C$  be the one-hot vector for class  $c$  and  $c_i = \arg \max_c \hat{S}_k^{(c)}(u_i, v_i)$ . The BEV tensor  $M_k^{\text{BEV}} \in \{0, 1\}^{H \times W \times C}$  (with  $C=20$  channels, one per class) is obtained by “splatting” points to cells with a per-cell reducer (e.g., max/majority):

$$M_k^{\text{BEV}}(i, j, :) \leftarrow \text{Agg}\{\mathbf{e}_{c_i} \mid (i, j) \text{ from (8)}\}. \quad (9)$$

For sequential inputs, BEV maps are temporally fused by exponential smoothing (EMA):

$$\tilde{M}_t^{\text{BEV}} = \alpha M_t^{\text{BEV}} + (1 - \alpha) \tilde{M}_{t-1}^{\text{BEV}}, \quad \alpha \in (0, 1], \quad (10)$$

where the fused BEV tensor  $\tilde{M}_t^{\text{BEV}} \in \mathbb{R}^{128 \times 256 \times 20}$  is then encoded by EfficientNet-B0 to yield  $f_t^{\text{BEV}}$ , which is fused with the RGB latent  $f_t^R$  for planning and control. Importantly, the BEV map  $\tilde{M}_t^{\text{BEV}}$  is further encoded by a second EfficientNet-B0 encoder, producing a compact latent feature  $f_t^{\text{BEV}}$ . This BEV feature is then fused with the RGB encoder latent feature  $f_t^R$  in the fusion block, forming the joint perception embedding  $\mathbf{z}_t$  that drives the planning and control module.

For simplicity, we do not perform ego-motion warping between frames; instead, the exponential decay term implicitly stabilizes the fused representation. The BEV generation assumes a locally planar ground, which is reasonable for most road and short-grass regions in our dataset. For strongly uneven or sloped terrain, this assumption introduces minor distortions, but these are mitigated by the temporal fusion that averages depth over multiple frames. In future work, incorporating pose-based spatial alignment and height-aware BEV encoding could further improve consistency in high-speed or non-planar motion.

**2) Planning and Control Part:** Let  $\mathbf{z}_t$  be the perception latent at time  $t$  concatenated with ancillary inputs (e.g., robot speed) and the *transformed* upcoming route points. A GRU models temporal dependencies:

$$\mathbf{r}_t = \sigma(\mathbf{W}_r[\mathbf{z}_t, \mathbf{h}_{t-1}] + \mathbf{b}_r), \quad (11)$$

$$\mathbf{u}_t = \sigma(\mathbf{W}_u[\mathbf{z}_t, \mathbf{h}_{t-1}] + \mathbf{b}_u), \quad (12)$$

$$\tilde{\mathbf{h}}_t = \tanh(\mathbf{W}_h[\mathbf{z}_t, \mathbf{r}_t \odot \mathbf{h}_{t-1}] + \mathbf{b}_h), \quad (13)$$

$$\mathbf{h}_t = (1 - \mathbf{u}_t) \odot \mathbf{h}_{t-1} + \mathbf{u}_t \odot \tilde{\mathbf{h}}_t, \quad (14)$$

where  $\sigma(\cdot)$  is the logistic function and  $\odot$  is the Hadamard product.

**PID controllers from waypoints.** From  $\mathbf{h}_t$  we predict incremental displacements  $\Delta \mathbf{w}_\ell = (\Delta x_\ell, \Delta y_\ell)$  and roll them for  $\ell = 1:N$  steps:

$$\Delta \mathbf{w}_\ell = \mathbf{W}^{(\ell)} \mathbf{h}_t + \mathbf{b}^{(\ell)}, \quad \ell = 1, \dots, N, \quad (15)$$

$$\hat{\mathbf{w}}_\ell = \hat{\mathbf{w}}_{\ell-1} + \Delta \mathbf{w}_\ell, \quad \hat{\mathbf{w}}_0 = (0, 0), \quad (16)$$

where waypoints  $\{\hat{\mathbf{w}}_\ell\}_{\ell=1}^N$  live in the local BEV frame. Then, we form an *aim point*  $\mathbf{a} = (\hat{\mathbf{w}}_1 + \hat{\mathbf{w}}_2)/2$  and derive heading and speed references:

$$\theta_{\text{ref}} = \text{atan2}(a_y, a_x), \quad (17)$$

$$v_{\text{ref}} = \gamma \|\hat{\mathbf{w}}_1 - \hat{\mathbf{w}}_2\|_2, \quad (18)$$

with a scale  $\gamma > 0$ . Let  $v$  be the measured linear speed. Lateral and longitudinal PID outputs are

$$u_{\text{lat}} = \text{PID}_{\text{lat}}(\theta_{\text{ref}} - \theta), \quad (19)$$

$$u_{\text{lon}} = \text{PID}_{\text{lon}}(v_{\text{ref}} - v). \quad (20)$$

We convert them into *position–orientation* control  $(x, y, \theta)$ , e.g., by a steering–throttle mapping:

$$u^{\text{PID}} = (x_{\text{PID}}, y_{\text{PID}}, \theta_{\text{PID}}) = \Psi(u_{\text{lat}}, u_{\text{lon}}). \quad (21)$$

### Algorithm 1: Control Policy (sketch)

---

**Input:** Perception latent  $\mathbf{z}_t$ , previous GRU state  $\mathbf{h}_{t-1}$ , route points  $(R_{p1}^x, R_{p2}^x)$   
**Output:** Control  $u_t = (x, y, \theta)$   
 Compute  $\mathbf{h}_t$  with GRU from  $\mathbf{z}_t$   
 Roll out waypoints  $\{\hat{\mathbf{w}}_\ell\}_{\ell=1}^N$   
 $u^{\text{PID}} \leftarrow \Psi(\text{PID}_{\text{lat/lon}}(\hat{\mathbf{w}}_{1:2}))$   
 Infer command  $C_t$  from  $(R_{p1}^x, R_{p2}^x)$   
 $u^{\text{MLP}} \leftarrow \text{MLP}_{C_t}(\mathbf{h}_t)$   
 Blend  $u^{\text{PID}}$  and  $u^{\text{MLP}}$  using Eq. (24)  
**return**  $u_t$

---

**Command-specific MLP controllers.** In parallel, *command-specific* MLPs infer control directly from  $\mathbf{h}_t$  (not from waypoints). We first infer a discrete command  $C_t \in \{\text{straight, left, right}\}$  from the upcoming two route points (in local coordinates  $(R_{p1}^x, R_{p2}^x)$ ), using simple thresholds:

$$C_t = \begin{cases} \text{left,} & R_{p1}^x \leq -\tau_1 \vee R_{p2}^x \leq -\tau_2, \\ \text{right,} & R_{p1}^x \geq \tau_1 \vee R_{p2}^x \geq \tau_2, \\ \text{straight,} & \text{otherwise.} \end{cases} \quad (22)$$

with an MLP head specific to  $C_t$  predicts

$$u^{\text{MLP}} = (x_{\text{MLP}}, y_{\text{MLP}}, \theta_{\text{MLP}}) = \text{MLP}_{C_t}(\mathbf{h}_t). \quad (23)$$

**Control blending policy.** The final control blends both controllers with confidence gating (threshold  $\epsilon > 0$ ) and weights  $\beta_{ij} \in [0, 1]$ :

$$\text{if } \|u^{\text{MLP}}\| \geq \epsilon \wedge \|u^{\text{PID}}\| \geq \epsilon : u_t = \begin{bmatrix} \beta_{00} & \beta_{10} \\ \beta_{01} & \beta_{11} \end{bmatrix} \begin{bmatrix} u^{\text{MLP}} \\ u^{\text{PID}} \end{bmatrix}; \quad (24)$$

$$\text{else if } \|u^{\text{MLP}}\| \geq \epsilon : u_t = u^{\text{MLP}}; \quad (25)$$

$$\text{else if } \|u^{\text{PID}}\| \geq \epsilon : u_t = u^{\text{PID}}; \quad (26)$$

$$\text{else : } u_t = \mathbf{0}, \quad (27)$$

where  $\beta_{ij}$  are task loss weight which are tuned adaptively during training process (see Subsection III-D). Algorithm 1 summarizes how the latent spaces from the perception encoder are translated into low-level control actions.

**3) Global-to-Local Transformation:** The model ingests, besides RGB-D and GNSS, a *sequence of route points* that prescribes the path from start to goal. At time  $t$ , we select the next two route points  $(\phi^{(1)}, \lambda^{(1)}), (\phi^{(2)}, \lambda^{(2)})$  (global lat–lon) and transform them to local Cartesian coordinates  $(R_{p1}^x, R_{p1}^y), (R_{p2}^x, R_{p2}^y)$  in the BEV frame where the robot sits at  $(0, 0)$  (bottom center).

First compute the bearing  $\beta$  from two consecutive robot GNSS positions  $(\phi_1, \lambda_1)$  and  $(\phi_2, \lambda_2)$ :

$$\beta = \text{atan2}(\sin \Delta \lambda \cos \phi_2, \cos \phi_1 \sin \phi_2 - \sin \phi_1 \cos \phi_2 \cos \Delta \lambda), \quad (28)$$

with  $\Delta \lambda = \lambda_2 - \lambda_1$ . To verify the robustness of GNSS-based bearing estimation, we compared it against IMU-based heading computed via an EKF filter, as shown in Fig. 2. In open-field trials, GNSS-based estimation (orange) achieved lower angular drift than IMU with EKF-based estimation

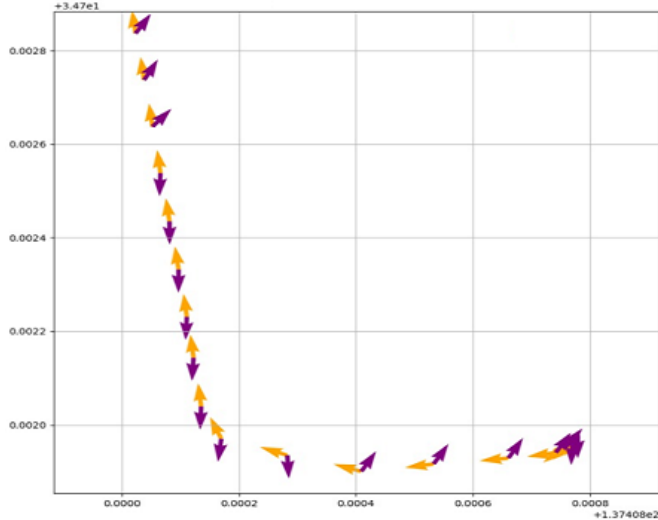


Fig. 2: GNSS-based bearing estimation (orange) vs 9-axis IMU with EKF-based bearing estimation (purple).



Fig. 3: The experiment area. Red: Old DeepIPC dataset coverage area. Blue: extended coverage area used for all models in this experiment. Yellow hollow circles represent a route that consists of start, finish, and a set of route points. (<https://goo.gl/maps/9rXobdhP3VYdjXn48>)

(purple), confirming its superior stability without magnetic interference. However, performance degraded near tall buildings due to partial satellite blockage, consistent with our qualitative observations. For a nearby route point  $(\phi_r, \lambda_r)$  and current robot fix  $(\phi_c, \lambda_c)$ , an equirectangular approximation yields the local offsets (meters)

$$\Delta x' = C_e \cos \phi_c (\lambda_r - \lambda_c), \quad \Delta y' = C_m (\phi_r - \phi_c), \quad (29)$$

$$\begin{bmatrix} R_p^x \\ R_p^y \end{bmatrix} = \begin{bmatrix} \cos \beta & -\sin \beta \\ \sin \beta & \cos \beta \end{bmatrix} \begin{bmatrix} \Delta x' \\ \Delta y' \end{bmatrix}, \quad (30)$$

where  $C_e$  and  $C_m$  are the local radii of curvature of the Earth ellipsoid at the current latitude  $\phi_c$ , given by

$$C_m = \frac{a(1 - e^2)}{(1 - e^2 \sin^2 \phi_c)^{3/2}}, \quad C_e = \frac{a}{\sqrt{1 - e^2 \sin^2 \phi_c}},$$

TABLE I: Statistics of the Seq-DeepIPC Dataset

Conditions	Sunny and Cloudy
Total routes	16 (train), 5 (validation), 5 (test)
$\mathcal{N}$ samples*	5164 (train), 1799 (val), 1681 (test)
Devices	Unitree Go2 Stereolabs Zed RGBD camera U-blox Zed-F9P GNSS receiver
Object classes	Following Cityscapes classes [28]

\* $\mathcal{N}$  samples is the number of observation sets. Each set consists of an RGBD image, GNSS location, and control signals.

with  $a$  the semi-major axis and  $e$  the eccentricity of the reference ellipsoid as in the WGS84 standard parameters, with  $a = 6378137\text{m}$  and  $e^2 = 0.00669437999014$ . This formulation accounts for the Earth's ellipsoidal shape, improving accuracy over the spherical approximation. It ensures precise projection of the route points into the local frame aligned with the BEV map. This alignment enables: (i) command inference from  $(R_{p1}^x, R_{p2}^x)$  (left/straight/right), and (ii) conditioning the GRU on the path heading relative to the robot.

### C. Dataset

The dataset for Seq-DeepIPC was collected at Toyohashi University of Technology, Japan, over an extended campus route that includes both structured road surfaces and unstructured grassy areas. Compared to the original DeepIPC dataset (shorter loop, mainly road surfaces), the new dataset covers a larger perimeter and more diverse conditions, which better reflects the challenges of legged robot navigation. A schematic of the experiment area is shown in Fig. 3. The area inside the red lines is the coverage area of the old DeepIPC dataset. Meanwhile, the area inside the blue lines is the extended coverage area used for all models in this experiment. The summary of the dataset information can be seen on Table I while the sensor placement on the legged robot can be seen on Fig. 4.

In total, the dataset consists of 26 distinct trajectories, partitioned into 16 routes for training, 5 routes for validation, and 5 routes for testing. Each trajectory contains synchronized multimodal streams:

- RGB images  $I_t^R$  and depth maps  $I_t^D$  captured at 30 FPS,
- GNSS measurements  $(\phi_t, \lambda_t)$  at 1 Hz,
- route point sequences  $\mathcal{P} = \{(\phi^{(m)}, \lambda^{(m)})\}$  that define the global path,
- expert control commands  $u_t = (x, y, \theta)$  recorded from teleoperation of the legged robot, and
- estimated forward velocity  $v_t$  computed from consecutive GNSS fixes:

$$v_t = \frac{d((\phi_{t-1}, \lambda_{t-1}), (\phi_t, \lambda_t))}{\Delta t}, \quad (31)$$

where  $d(\cdot, \cdot)$  is the great-circle distance and  $\Delta t$  is the GNSS sampling interval.

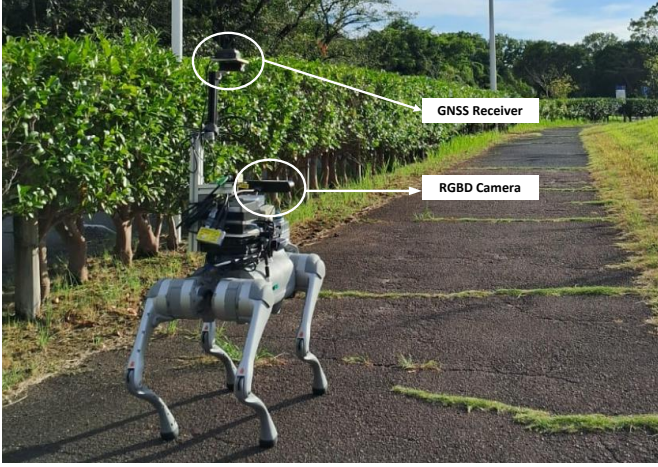


Fig. 4: Sensor placement on the legged robot (Unitree Go2).

**Ground-truth construction.** The ground-truth waypoints are extracted from the robot’s actual traversal trajectory during data collection. This trajectory is estimated using a visual–inertial odometry (VIO) algorithm integrated into the robot’s on-board edge device, providing locally consistent 6-DoF motion estimates. To be noted, we only consider 5 future waypoints to be predicted; they only have a gap of around 5 meters (between the robot’s current location to the fifth waypoint). Thus, VIO was preferred for trajectory ground-truth construction because it provides denser and locally more consistent data than GNSS, which can suffer from signal degradation and update delays. While GNSS is used for heading estimation during deployment, VIO yields smoother reference trajectories for supervised waypoint prediction.

The ground-truth position–orientation controls  $(x, y, \theta)$  correspond to the remote control states issued during teleoperation, ensuring that the model learns from human-expert steering actions. Depth supervision uses the synchronized RGB-D measurements  $I_t^D$ , whereas semantic segmentation ground truth is obtained using the pretrained SegFormer [29] model. SegFormer, trained on the Cityscapes dataset [28], provides strong generalization to outdoor scenes and acts as a “teacher” model in a knowledge-distillation manner, where Seq-DeepIPC serves as the “student”.

To ensure temporal consistency, frames are grouped into short observation windows of length  $K \in \{1, 2, 3\}$ , producing training samples of the form

$$(O_t, P_t, g_t; S_t, D_t, W_t, u_t), \quad (32)$$

where  $O_t$  is the sequence of RGB-D images,  $P_t$  the sequence of route points that will be transformed into local coordinates,  $g_t$  is the sequence of GNSS measurements, and  $\{S_t, D_t, W_t, u_t\}$  are the ground-truth labels supervising the multi-task outputs.

#### D. Training Configuration

We train Seq-DeepIPC using supervised imitation learning on a PC equipped with an RTX 4090 GPU. The model that achieves the lowest validation  $\mathcal{L}_{\text{total}}$  is selected for testing. We

adopt the AdamW optimizer with  $(\beta_1, \beta_2) = (0.9, 0.999)$ , an initial learning rate of  $\eta_0 = 10^{-4}$ , and weight decay of  $10^{-4}$ . The batch size is set to 5. Training continues until early stopping is triggered when the validation  $\mathcal{L}_{\text{total}}$  shows no improvement for 30 consecutive epochs. The learning rate follows a step decay schedule: if no improvement occurs for 5 epochs, the learning rate is halved, following  $\eta \leftarrow \max(0.5\eta, \eta_{\min})$  with  $\eta_{\min} = 10^{-6}$ . The sequence length for temporal inputs is  $K \in \{1, 2, 3\}$ .

**Overall training objective.** The total loss combines perception, waypoint, and control objectives. The overall loss is a weighted sum of task-specific losses:

$$\mathcal{L}_{\text{total}} = \alpha_{\text{percep}} \mathcal{L}_{\text{percep}} + \alpha_{\text{wp}} \mathcal{L}_{\text{wp}} + \alpha_{\text{ctrl}} \mathcal{L}_{\text{ctrl}}, \quad (33)$$

where the task weights  $\alpha_{\{\cdot\}}$  are automatically tuned using Modified Gradient Normalization (MGN) [30] as in DeepIPC. This ensures equitable gradient magnitudes across tasks, preventing dominance by any single loss and promoting stable multi-task learning.

**Segmentation loss:** Semantic segmentation is trained using an additive combination of Binary Cross-Entropy (BCE) and Dice loss:

$$\mathcal{L}_{\text{seg}} = \text{BCE}(\hat{S}, S) + \text{Dice}(\hat{S}, S), \quad (34)$$

where

$$\text{BCE}(\hat{S}, S) = -\frac{1}{N} \sum_{i=1}^N (S_i \log \hat{S}_i + (1-S_i) \log(1-\hat{S}_i)), \quad (35)$$

$$\text{Dice}(\hat{S}, S) = 1 - \frac{2 \sum_i \hat{S}_i S_i + \epsilon}{\sum_i \hat{S}_i + \sum_i S_i + \epsilon}. \quad (36)$$

The BCE term encourages pixel-wise classification accuracy and is particularly effective for well-balanced regions, while the Dice loss improves overlap-based similarity, mitigating class imbalance and emphasizing small or thin structures in the scene. The combination allows the network to optimize both global segmentation consistency and region-wise precision.

**Depth loss:** Depth estimation is optimized using a combination of  $\ell_1$  and  $\ell_2$  norms:

$$\mathcal{L}_{\text{depth}} = \|\hat{D} - D\|_1 + \|\hat{D} - D\|_2^2. \quad (37)$$

The  $\ell_1$  component enforces robustness against outliers and preserves local discontinuities (e.g., edges and object boundaries), whereas the  $\ell_2$  term penalizes large residuals more strongly, encouraging overall smoothness and stable convergence. Their combination balances detail preservation and global consistency, which is critical for learning depth maps that support reliable BEV projection.

**Perception loss:** The perception branch jointly optimizes both segmentation and depth estimation objectives:

$$\mathcal{L}_{\text{percep}} = \mathcal{L}_{\text{seg}} + \mathcal{L}_{\text{depth}}. \quad (38)$$

This multi-task formulation enables the encoder to learn shared spatial representations that improve downstream control and planning accuracy.

TABLE II: Model Specification

Model	Total Parameters ↓	Model Size ↓	Input/Sensor	Output
Huang et al. [9]	74953360	300.2 MB	RGBD, High-level commands	Segmentation, Low-level Controls
AIM-MT [10]	27967063	112.1 MB	RGB, GNSS	Segmentation, Depth, Waypoints
DeepIPC [11]	20953266	85.0 MB	RGBD, GNSS	Segmentation, BEV Semantic, Waypoints, Low-level Controls
Seq-DeepIPC	12291227	47.5 MB	RGBD, GNSS	Segmentation, Depth, BEV Semantic, Waypoints, Low-level Controls

We implement Huang et al.'s model [9] based on their paper. Meanwhile, AIM-MT [10] and DeepIPC [11] are implemented based on author's original repository that can be accessed at <https://github.com/autonomousvision/neat> and <https://github.com/oskarnatan/DeepIPC> with a small modification for controlling a legged robot. All models are deployed on a Jetson AGX Orin.

*Waypoint and control losses:* Both waypoint regression and control prediction are formulated as continuous regression tasks, optimized using a combination of  $\ell_1$  and  $\ell_2$  losses:

$$\mathcal{L}_{\text{wp}} = \|\hat{W} - W\|_1 + \|\hat{W} - W\|_2^2, \quad (39)$$

$$\mathcal{L}_{\text{ctrl}} = \|\hat{u} - u\|_1 + \|\hat{u} - u\|_2^2. \quad (40)$$

The  $\ell_1$  component provides robustness to noisy teleoperation labels and occasional trajectory deviations, ensuring stable learning from imperfect demonstrations, while the  $\ell_2$  term enforces smooth convergence and penalizes large prediction errors in position and orientation. This dual objective allows the controller to maintain both trajectory precision and smooth actuation responses which are critical properties for legged locomotion in unstructured terrain.

### E. Evaluation Settings

We adopt both offline and online evaluations. Offline tests provide quantitative accuracy while online tests verify qualitative behavior on the real legged robot.

**Offline tests.** We compare Seq-DeepIPC against some latest models named *DeepIPC* [11], *AIM-MT* [10], and *Huang et al.* [9], adapted to consume the same inputs as ours. The model specification details can be seen on Table II. It shows that our proposed model, Seq-DeepIPC is lighter than other models in terms of number of trainable parameters and model size. Since not all models predict the same outputs (e.g., DeepIPC does not predict depth), comparisons are reported task-wise rather than in a single aggregate metric. We also ablate the sequence length  $K \in \{1, 2, 3\}$ . All models are evaluated on the 5 held-out test routes using metrics: segmentation IoU, depth MAE, waypoint MAE, and control MAE.

*Segmentation IoU:* Let  $\mathcal{C}$  be the set of semantic classes and  $\Omega$  the pixel domain. For class  $c \in \mathcal{C}$ , with ground truth  $S^{(c)} \in \{0, 1\}^\Omega$  and prediction  $\hat{S}^{(c)} \in [0, 1]^\Omega$  thresholded to  $\{0, 1\}$ ,

$$\text{IoU}_c = \frac{|\hat{S}^{(c)} \cap S^{(c)}|}{|\hat{S}^{(c)} \cup S^{(c)}|}, \quad (41)$$

and the IoU is

$$\text{IoU} = \frac{1}{|\mathcal{C}|} \sum_{c \in \mathcal{C}} \text{IoU}_c. \quad (42)$$

*Depth MAE:* For per-pixel depth  $D, \hat{D} \in \mathbb{R}^\Omega$  (meters),

$$\text{MAE}_{\text{depth}} = \frac{1}{|\Omega|} \sum_{p \in \Omega} |\hat{D}(p) - D(p)|. \quad (43)$$

*Waypoint MAE:* Given  $N$  local waypoints,  $W = \{\mathbf{w}_\ell\}_{\ell=1}^N$  and  $\hat{W} = \{\hat{\mathbf{w}}_\ell\}_{\ell=1}^N$ ,

$$\text{MAE}_{\text{wp}} = \frac{1}{N} \sum_{\ell=1}^N \|\hat{\mathbf{w}}_\ell - \mathbf{w}_\ell\|_1. \quad (44)$$

*Control MAE:* For robot control  $u = (x, y, \theta) \in \mathbb{R}^3$ ,

$$\text{MAE}_{\text{ctrl}} = \frac{1}{3} (|\hat{x} - x| + |\hat{y} - y| + |\hat{\theta} - \theta|). \quad (45)$$

**Online tests (qualitative).** We deploy Seq-DeepIPC on a Unitree legged robot across predefined campus routes that include both asphalt roads and grassy terrain. Unlike the wheeled platform used in DeepIPC, the legged robot can safely traverse uneven and semi-structured surfaces without manual intervention. We further analyze challenging conditions such as partial GNSS occlusion near tall buildings. In these regions, satellite signal degradation perturbs the bearing estimation and consequently the global-to-local coordinate transformation, resulting in gradual navigation drift. Qualitative evaluation focuses on visualizing the full perception-to-control pipeline, including RGB inputs, predicted segmentation and depth maps, BEV projections, planned waypoints, and  $(x, y, \theta)$  control traces overlaid with the ground-truth GNSS trajectory. These visualizations reveal that Seq-DeepIPC produces temporally consistent segmentations and smooth waypoint transitions, leading to stable locomotion even under texture variation and illumination changes. Qualitative results are discussed in more detail in Sec. IV-D.

## IV. RESULTS AND DISCUSSION

We comprehensively evaluate Seq-DeepIPC and three baselines: DeepIPC, AIM-MT, and Huang—through both offline quantitative analysis and online real-world deployment. Offline evaluation assesses perception and control using four metrics: IoU for segmentation and MAE for depth, waypoint, and control outputs  $(x, y, \theta)$ . Each model is trained and tested three times with randomized seeds, and mean  $\pm$  std values are reported for statistical reliability. The consolidated quantitative results are summarized in Table III. Online evaluation further deploys the best-performing Seq-DeepIPC on a Unitree Go2 legged robot operating on both asphalt and grass terrains, using live RGB-D and GNSS inputs processed on a Jetson AGX Orin. Qualitative outcomes, shown in Fig. 5, confirm that Seq-DeepIPC can maintain smooth navigation and robust perception across heterogeneous real-world environments.

**TABLE III:** Quantitative comparison of Seq-DeepIPC and baselines. Results are reported as mean  $\pm$  standard deviation across three runs. Best values in each column are highlighted in bold.

Model	Seq Input	Seg. IoU $\uparrow$	Depth MAE $\downarrow$	WP MAE $\downarrow$	Ctrl MAE $\downarrow$
Huang [9]	1	$0.814 \pm 0.003$	—	—	$0.061 \pm 0.001$
	2	$0.807 \pm 0.005$	—	—	$0.060 \pm 0.001$
	3	$0.809 \pm 0.003$	—	—	$0.062 \pm 0.004$
AIM-MT [10]	1	$0.847 \pm 0.004$	$0.091 \pm 0.002$	$0.710 \pm 0.025$	—
	2	$0.836 \pm 0.018$	$0.090 \pm 0.001$	$0.713 \pm 0.015$	—
	3	$0.842 \pm 0.003$	$0.091 \pm 0.003$	<b><math>0.714 \pm 0.026</math></b>	—
DeepIPC [11]	1	$0.839 \pm 0.002$	—	$0.770 \pm 0.017$	$0.055 \pm 0.003$
	2	$0.839 \pm 0.004$	—	$0.739 \pm 0.033$	$0.057 \pm 0.007$
	3	<b><math>0.847 \pm 0.001</math></b>	—	$0.729 \pm 0.019$	$0.047 \pm 0.001$
Seq-DeepIPC	1	$0.839 \pm 0.003$	$0.088 \pm 0.005$	$0.774 \pm 0.039$	$0.063 \pm 0.009$
	2	$0.837 \pm 0.006$	$0.087 \pm 0.003$	$0.730 \pm 0.019$	$0.058 \pm 0.002$
	3	$0.844 \pm 0.002$	<b><math>0.084 \pm 0.001</math></b>	$0.725 \pm 0.010$	<b><math>0.046 \pm 0.001</math></b>

### A. Ablation Study and Sequential Effects

**Impact of sequential inputs.** The number of sequential frames  $K$  markedly affects models with temporal encoders (DeepIPC, Seq-DeepIPC) but not those lacking explicit recurrence (AIM-MT, Huang). As shown in Table III, increasing  $K$  from 1 to 3 yields monotonic gains in IoU, depth accuracy, waypoint precision, and control smoothness for both DeepIPC variants. This trend empirically confirms that the GRU-based latent integration captures temporal continuity across frames, suppressing per-frame perception noise (e.g., short occlusions). In contrast, Huang and AIM-MT process stacked frames independently; thus, temporal redundancy provides little additional information and may even cause feature over-smoothing. The results highlight that merely feeding sequential frames is insufficient—architectural mechanisms must translate temporal correlation into stable latent state.

**Temporal dynamics and control stability.** Seq-DeepIPC’s GRU stabilizes the latent representations by integrating temporal dependencies across consecutive RGB-D frames. As a result, the latent features fed to the control policy are temporally consistent, reducing erratic command outputs. In practice, this temporal coherence suppresses overreactive PID corrections and leads to more stable actuation, particularly in mixed-terrain navigation where both visual and depth signals exhibit higher variance. Quantitatively, the reduction in control MAE from  $K=1$  to  $K=3$  is the most significant among all ablation settings. This suggests that Seq-DeepIPC does not merely memorize local transitions but effectively models short-term dynamics for perception stability and motion smoothness.

### B. Effect of Multi-Task Perception

Seq-DeepIPC’s dual supervision encourages the encoder to preserve geometry-aware features useful for both perception and planning. The auxiliary loss leads to latent spaces with improved spatial consistency. Empirically, this yields higher control accuracy and smoother waypoint transitions. The improvement suggests that implicit geometry learning acts as a structural prior that reinforces semantics-to-geometry alignment. Furthermore, by jointly learning segmentation and depth estimation, the model disentangles texture and structural cues,

enabling better obstacle boundary awareness and traversability reasoning. The joint segmentation–depth learning also reduces over-fitting: gradients from the two tasks balance semantic and geometric fidelity. This complementary effect explains why Seq-DeepIPC consistently outperforms DeepIPC, particularly when sequential information is abundant ( $K=3$ ). Depth estimation forces the encoder to exploit subtle photometric cues, while segmentation enforces semantic boundary awareness. Together, they produce robust features that generalize across terrain textures which is essential for accurate navigation.

### C. Task-Wise Comparative Analysis.

**Perception accuracy** AIM-MT, DeepIPC, and Seq-DeepIPC achieve significantly higher IoU than Huang, confirming the benefit of multi-task and feature-fusion. Despite employing a lightweight EfficientNet-B0 encoder, Seq-DeepIPC maintains near state-of-the-art IoU, validating that its temporal and depth cues effectively compensate for reduced model size. The sequential variant produces more stable segmentation boundaries and fewer transient misclassifications across frames. This stability stems from GRU-based temporal smoothing, which suppresses frame-to-frame fluctuations. The predicted segmentation masks exhibit sharper object contours, better-defined ground regions and cleaner obstacle separation. Furthermore, depth supervision enriches the encoder’s latent geometry, improving the delineation of traversable versus non-traversable areas. These findings indicate that dual-head supervision promotes semantically coherent and geometry-consistent spatial reasoning.

**Waypoint regression.** AIM-MT excels in waypoint prediction. However, Seq-DeepIPC narrows this gap as the input sequence length  $K$  increases, benefiting from temporally fused latent embeddings that capture local motion continuity and long-term orientation cues. The GRU implicitly models short-horizon trajectory evolution, generating smoother waypoint transitions even without explicit attention or motion priors. Unlike single-frame models, which rely solely on instantaneous appearance cues, Seq-DeepIPC leverages motion-consistent features across frames to reduce waypoint displacement variance. This advantage becomes pronounced

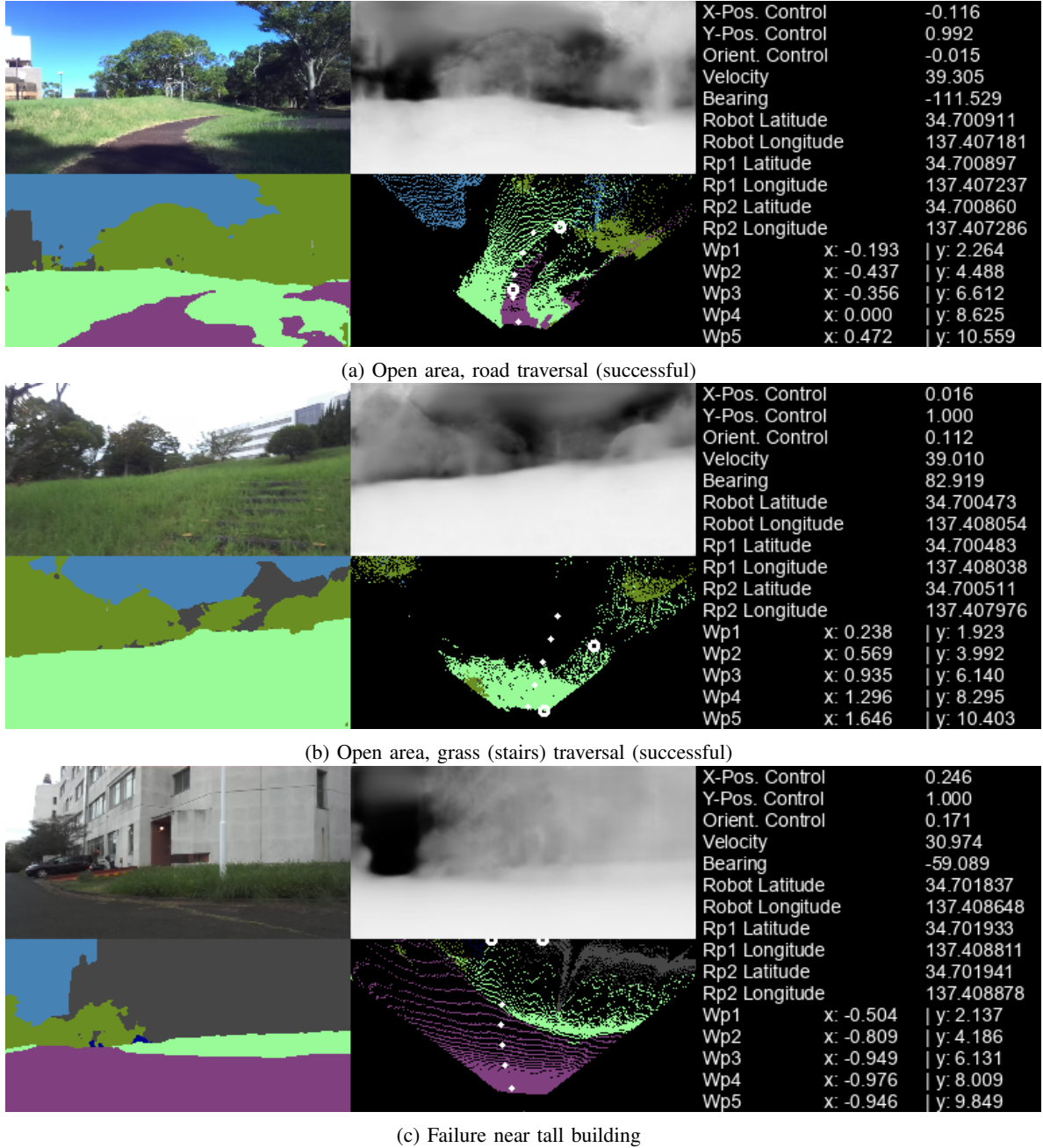


**Fig. 5:** Qualitative results of Seq-DeepIPC deployment on a Unitree legged robot. Each row corresponds to an observation set, showing representative outputs. Negative x-pos and orient. controls mean to the left, while positive means to the right. (a) Successful road traversal, (b) successful grass (stairs) traversal, (c) failure case near tall buildings, as the model fails to predict waypoints correctly due to misplaced route points.

in unstructured areas where the robot's orientation changes frequently and texture cues are sparse. Empirically, the waypoint MAE decreases monotonically with sequence length, confirming that temporal modeling provides an efficient approximation. These results suggest that Seq-DeepIPC's temporal recurrence generalizes effectively to natural terrains.

**Control precision.** Both DeepIPC and Seq-DeepIPC outperform Huang in control MAE, demonstrating the importance of direct perception-to-control coupling. Seq-DeepIPC's joint perception branch links high-level semantic and depth features to low-level control dynamics, enabling context-aware motion

responses. The geometry-informed latent representations enhance the model's sensitivity to slope changes and surface irregularities, producing smoother velocity and orientation regulation. Temporal GRU fusion further stabilizes these signals by filtering short-term fluctuations in perception output, reducing oscillations in the control loop. As a result, the robot exhibits fewer heading reversals and less jitter in angular velocity, particularly during transitions between road and grass surfaces. Empirically, the control MAE reduction from  $K=1$  to  $K=3$  reflects more reliable policy consistency and reduced PID correction overhead.

#### D. Qualitative Evaluation and Failure Analysis

The qualitative cases in Fig. 5 illustrate typical operational scenarios. In open environments, the robot accurately distinguishes road and grass regions, with consistent segmentation and depth predictions over consecutive frames. The BEV map remains coherent, producing smooth waypoint trajectories and stable control commands. In contrast, near tall structures, GNSS errors distort the geodesic bearing used for coordinate transformation, yielding misplaced route points and misaligned control vectors that navigate the robot. These results emphasize that the remaining bottleneck is not visual perception but external localization reliability. Such systematic errors can be mitigated by fusing GNSS with other robust sensors, applying temporal filtering of the absolute heading estimate, or adopting confidence-weighted waypoint sampling.

Online tests reveal that Seq-DeepIPC performs reliably in open areas, even under moderate illumination and weather variations. However, its dependence on GNSS-only bearing estimation causes localization drift near tall buildings, where multipath interference corrupts coordinate transformation. The resulting misalignment between global route points and local BEV grids leads to control offset. Importantly, perception quality remains intact, isolating the error source to global-local misprojection rather than network instability. Overall, Seq-DeepIPC demonstrates that *temporal, geometric, and semantic integration* can jointly elevate end-to-end robot navigation performance. It establishes a practical framework for extending perception-control coupling from wheeled to legged robots that can traverse in a more diverse environment.

#### V. CONCLUSION

This paper presented Seq-DeepIPC, a sequential and multi-task end-to-end perception-to-control framework for legged robot navigation in mixed-terrain environments. Building on DeepIPC, the model processes temporal RGB-D sequences through a lightweight encoder with dual-head perception for semantic segmentation and depth estimation. The outputs are projected into a bird's-eye-view (BEV) map and fused by a GRU-based planner to produce geometry-aware control commands. Experiments show that temporal integration and depth supervision improve perception consistency, waypoint accuracy, and control stability. By coupling sensor fusion and control through learning, Seq-DeepIPC bridges the gap between intelligent sensing and autonomous decision-making.

The results highlight three core findings: (i) temporal recurrence enhances motion continuity and reduces perception noise, (ii) geometry-aware auxiliary supervision strengthens spatial reasoning, and (iii) balanced multi-task learning ensures stable convergence. Beyond quantitative gains, Seq-DeepIPC extends end-to-end navigation from wheeled to legged robot, demonstrating robust performance across road and grass terrains. Although GNSS-only heading estimation remains sensitive near tall structures, the system performs reliably in open environments, suggesting the potential of integrating GNSS with other robust sensors for improved resilience. Future work will explore adaptive temporal fusion, multi-modal sensing, and broader deployment on diverse robotic platforms to advance real-world autonomy.

#### REFERENCES

- [1] X. Ding, J. Guo, Z. Ren, and P. Deng, “State-of-the-art in perception technologies for collaborative robots,” *IEEE Sensors Journal*, vol. 22, no. 18, pp. 17 635–17 645, 2022.
- [2] P. S. Chib and P. Singh, “Recent advancements in end-to-end autonomous driving using deep learning: A survey,” *IEEE Transactions on Intelligent Vehicles*, vol. 9, no. 1, pp. 103–118, 2024.
- [3] M. Aizat, N. Qistina, and W. Rahiman, “A comprehensive review of recent advances in automated guided vehicle technologies: Dynamic obstacle avoidance in complex environment toward autonomous capability,” *IEEE Transactions on Instrumentation and Measurement*, vol. 73, pp. 1–25, 2024.
- [4] O. Natan and J. Miura, “End-to-end autonomous driving with semantic depth cloud mapping and multi-agent,” *IEEE Transactions on Intelligent Vehicles*, vol. 8, no. 1, pp. 557–571, 2023.
- [5] W. Wu, X. Deng, P. Jiang, S. Wan, and Y. Guo, “Crossfuser: Multi-modal feature fusion for end-to-end autonomous driving under unseen weather conditions,” *IEEE Transactions on Intelligent Transportation Systems*, vol. 24, no. 12, pp. 14 378–14 392, 2023.
- [6] J. Du, Y. Bai, Y. Li, J. Geng, Y. Huang, and H. Chen, “Evolutionary end-to-end autonomous driving model with continuous-time neural networks,” *IEEE/ASME Transactions on Mechatronics*, vol. 29, no. 4, pp. 2983–2990, 2024.
- [7] J. Zhang, Q. Su, B. Tang, C. Wang, and Y. Li, “Dpsnet: Multitask learning using geometry reasoning for scene depth and semantics,” *IEEE Transactions on Neural Networks and Learning Systems*, vol. 34, no. 6, pp. 2710–2721, 2023.
- [8] R. Pei, S. Deng, L. Zhou, H. Qin, and Q. Liang, “Mcs-resnet: A generative robot grasping network based on rgb-d fusion,” *IEEE Transactions on Instrumentation and Measurement*, vol. 74, pp. 1–12, 2025.
- [9] Z. Huang, C. Lv, Y. Xing, and J. Wu, “Multi-modal sensor fusion-based deep neural network for end-to-end autonomous driving with scene understanding,” *IEEE Sensors Journal*, vol. 21, no. 10, pp. 11 781–11 790, 2021.
- [10] K. Chitta, A. Prakash, and A. Geiger, “Neat: Neural attention fields for end-to-end autonomous driving,” in *2021 IEEE/CVF International Conference on Computer Vision (ICCV)*, 2021, pp. 15 773–15 783.
- [11] O. Natan and J. Miura, “Deepipe: Deeply integrated perception and control for an autonomous vehicle in real environments,” *IEEE Access*, vol. 12, pp. 49 590–49 601, 2024.
- [12] M. Tan and Q. Le, “Efficientnetv2: Smaller models and faster training,” in *Proceedings of the 38th International Conference on Machine Learning*, ser. Proceedings of Machine Learning Research, M. Meila and T. Zhang, Eds., vol. 139. PMLR, 18–24 Jul 2021, pp. 10 096–10 106.
- [13] C. Lammie, A. Olsen, T. Carrick, and M. Rahimi Azghadi, “Low-power and high-speed deep fpga inference engines for weed classification at the edge,” *IEEE Access*, vol. 7, pp. 51 171–51 184, 2019.
- [14] K. Ishihara, A. Kanervisto, J. Miura, and V. Hautamaki, “Multi-task learning with attention for end-to-end autonomous driving,” in *2021 IEEE/CVF International Conference on Computer Vision and Pattern Recognition Workshops (CVPRW)*, Nashville, USA, Jun. 2021, pp. 2896–2905.
- [15] C. Hou and W. Zhang, “End-to-end urban autonomous driving with safety constraints,” *IEEE Access*, vol. 12, pp. 132 198–132 209, 2024.
- [16] J. K. Wang, X. Q. Ding, H. Xia, Y. Wang, L. Tang, and R. Xiong, “A lidar based end to end controller for robot navigation using deep neural network,” in *2017 IEEE International Conference on Unmanned Systems (ICUS)*, 2017, pp. 614–619.
- [17] K. Chitta, A. Prakash, B. Jaeger, Z. Yu, K. Renz, and A. Geiger, “Transfuser: Imitation with transformer-based sensor fusion for autonomous driving,” *IEEE Transactions on Pattern Analysis and Machine Intelligence*, vol. 45, no. 11, pp. 12 878–12 895, 2023.
- [18] X. Jia, P. Wu, L. Chen, J. Xie, C. He, J. Yan, and H. Li, “Think twice before driving: Towards scalable decoders for end-to-end autonomous driving,” in *2023 IEEE/CVF Conference on Computer Vision and Pattern Recognition (CVPR)*, 2023, pp. 21 983–21 994.
- [19] W. Wu, X. Deng, P. Jiang, S. Wan, and Y. Guo, “Crossfuser: Multi-modal feature fusion for end-to-end autonomous driving under unseen weather conditions,” *IEEE Transactions on Intelligent Transportation Systems*, vol. 24, no. 12, pp. 14 378–14 392, 2023.
- [20] Z. Huang, S. Sun, J. Zhao, and L. Mao, “Multi-modal policy fusion for end-to-end autonomous driving,” *Information Fusion*, vol. 98, p. 101834, 2023.
- [21] S. Azam, F. Munir, V. Kyrki, T. P. Kucner, M. Jeon, and W. Pedrycz, “Exploring contextual representation and multi-modality for end-to-end

autonomous driving,” *Engineering Applications of Artificial Intelligence*, vol. 135, p. 108767, 2024.

[22] S. Huch, F. Sauerbeck, and J. Betz, “Deepstep - deep learning-based spatio-temporal end-to-end perception for autonomous vehicles,” in *2023 IEEE Intelligent Vehicles Symposium (IV)*, 2023, pp. 1–8.

[23] A. Agrawal, S. Chen, A. Rai, and K. Sreenath, “Vision-aided dynamic quadrupedal locomotion on discrete terrain using motion libraries,” in *2022 International Conference on Robotics and Automation (ICRA)*, 2022, pp. 4708–4714.

[24] G. Deng, J. Luo, C. Sun, D. Pan, L. Peng, N. Ding, and A. Zhang, “Vision-based navigation for a small-scale quadruped robot pegasus-mini,” in *2021 IEEE International Conference on Robotics and Biomimetics (ROBIO)*, 2021, pp. 893–900.

[25] S. Cai, A. Ram, Z. Gou, M. A. W. Shaikh, Y.-A. Chen, Y. Wan, K. Hara, S. Zhao, and D. Hsu, “Navigating real-world challenges: A quadruped robot guiding system for visually impaired people in diverse environments,” ser. CHI ’24, New York, NY, USA, 2024.

[26] M. Schilling, J. Paskarbeit, H. Ritter, A. Schneider, and H. Cruse, “From adaptive locomotion to predictive action selection – cognitive control for a six-legged walker,” *IEEE Transactions on Robotics*, vol. 38, no. 2, pp. 666–682, 2022.

[27] S. Fahmi, V. Barasol, D. Esteban, O. Villarreal, and C. Semini, “Vital: Vision-based terrain-aware locomotion for legged robots,” *IEEE Transactions on Robotics*, vol. 39, no. 2, pp. 885–904, 2023.

[28] M. Cordts, M. Omran, S. Ramos, T. Rehfeld, M. Enzweiler, R. Benenson, U. Franke, S. Roth, and B. Schiele, “The cityscapes dataset for semantic urban scene understanding,” in *2016 IEEE Conference on Computer Vision and Pattern Recognition (CVPR)*, 2016, pp. 3213–3223.

[29] E. Xie, W. Wang, Z. Yu, A. Anandkumar, J. M. Alvarez, and P. Luo, “Segformer: Simple and efficient design for semantic segmentation with transformers,” in *Neural Information Processing Systems (NeurIPS)*, 2021.

[30] O. Natan and J. Miura, “Towards compact autonomous driving perception with balanced learning and multi-sensor fusion,” *IEEE Transactions on Intelligent Transportation Systems*, vol. 23, no. 9, pp. 16 249–16 266, 2022.



**Oskar Natan** (Member, IEEE) received his B.A.Sc. degree in Electronics Engineering and M.Eng. degree in Electrical Engineering from Politeknik Elektronika Negeri Surabaya, Indonesia, in 2017 and 2019, respectively. In 2023, he received his Ph.D.(Eng.) degree in Computer Science and Engineering from Toyohashi University of Technology, Japan. Since January 2020, he has been affiliated with the Department of Computer Science and Electronics, Universitas Gadjah Mada, Indonesia, first as a Lecturer and currently serves as an Assistant Professor. He has been serving as a reviewer/TPC member for some reputable journals and conferences. His research interests lie in the fields of deep learning, sensor fusion, hardware acceleration, and end-to-end systems.



**Jun Miura** (Member, IEEE) received his B.Eng. degree in Mechanical Engineering and his M.Eng. and Dr.Eng. degrees in Information Engineering from the University of Tokyo, Japan, in 1984, 1986, and 1989, respectively. From 1989 to 2007, he was with the Department of Computer-controlled Mechanical Systems, Osaka University, Japan, first as a Research Associate and later as an Associate Professor. From March 1994 to February 1995, he served as a Visiting Scientist at the Department of Computer

Science, Carnegie Mellon University, USA. In 2007, he became a Professor at the Department of Computer Science and Engineering, Toyohashi University of Technology, Japan, where he remains to the present. To date, he has received plenty of awards and authored or co-authored more than 265 peer-reviewed scientific articles in the field of robotics and autonomous systems in internationally reputable journals and conferences.